Universal micro-trench resonators for monolithic integration with silicon waveguides

Philippe Jean, Alexandre Douaud, Souleymane Toubou Bah, Sophie LaRochelle, Younès Messaddeq, and Wei Shi

Universal micro-trench resonators for monolithic integration with silicon waveguides

PHILIPPE JEAN,[1,2] ALEXANDRE DOUAUD,[1] SOULEYMANE TOUBOU BAH,[1] SOPHIE LAROCHELLE,[1,2] YOUNÈS MESSADDEQ,[1,3] AND WEI SHI[1,2,*]

[1]*Centre d'Optique, Photonique et Laser (COPL), 2375 rue de la Terrasse, Université Laval, Québec, G1V 0A6, Canada*
[2]*Département de Génie Électrique et de Génie Informatique, Université Laval, 2325, rue de l'Université, Québec, G1V 0A6, Canada*
[3]*Département de Physique, de Génie Physique et d'Optique, Université Laval, 2325, rue de l'Université, Québec, G1V 0A6, Canada*
*wei.shi@gel.ulaval.ca

Abstract: We present a systematic study of micro-trench resonators for heterogeneous integration with silicon waveguides. We experimentally and numerically demonstrate that the approach is compatible with a large variety of thin film materials and that it does not require specific etching recipe development, thus making it virtually universal. The microresonators are fabricated through in-foundry silicon-on-insulator processing and in-house backend processing. We also report ultra-compact chalcogenide microresonators with radius as small as 5μ and quality factors up to 1.8×10^5. We finally show a proof-of-concept of a novel multilayer waveguide using the micro-trench technique.

1. Introduction

The use of silicon-on-insulator (SOI) has rapidly increased in the last decade or so, both for research and industrial applications. The platform now enables all optical functionalities on compact chips operating at telecommunication wavelengths. The strong index contrast between silicon ($n_{Si} = 3.47$) and its oxide ($n_{SiO_2} = 1.44$) allows for densely integrated structures with over a thousand miniaturized optical components on a single chip [1]. The integration density and compatibility with state-of-the-art microfabrication technologies make SOI relevant even in the face of emerging platforms that offers improved performances like lithium niobate for electro-optic modulation [2] or silicon nitride for nonlinear photonics [3]. The maturity of SOI was reached through intensive research efforts that were mainly driven by telecommunications [4]. Foundries worldwide now offer streamlined access to their process with well-developed design kits [5]. Emerging platforms will have to go through similar developmental steps to reach a comparable level of maturity. An attractive approach to accelerate the use of new materials while retaining the advantages of SOI is to combine them using an heterogeneous integration scheme. There is then a need to devise innovative methods to integrate advanced materials on SOI without compromising the in-foundry fabrication or the high integration density.

Here the term heterogeneous integration is used to describe the combination of non-silicon materials directly on SOI chips in a monolithic fashion, in contrast with hybrid integration that could use external components. An optimal heterogeneous integration method should accommodate various materials without requiring significant modification of the process flow. Also, the limited list of CMOS-compatible materials justify the development of methods that can be done in external dedicated foundries as a back-end process. It's also important for an integration method to retain the advantages of SOI as much as possible; mainly the high integration density and CMOS compatibility. A solution combining these requirements is

micro-trench filling, where waveguides are defined by etching micro-trenches in the SOI silica top cladding [6,7]. These molds are then filled with a thin film of amorphous material. The process is depicted in Fig. 1(a). The restrictions on the material that can be used with this method are relaxed; the lower boundary on the refractive index is set by the guiding condition with the silica cladding ($n>1.44$) while there is practically no upper bound. These structures can be interfaced with silicon waveguides by evanescent coupling on the same layer [6] or on vertically stacked layers [8]. This approach was first demonstrated by Bradley et al. in 2014 to integrate rare-earth doped aluminium oxide (Al_2O_3) films with silicon nitride waveguides to create low-threshold microlasers [9]. The versatility of the method was later outlined through the use of various rare-earth ions to achieve microlasers operating at different wavelengths [10]. Since then, Su et al. have reported in-depth simulations and characterization of Al_2O_3/Si_3N_4 microcavities with quality factors of $Q>1 \times 10^6$. Frankis et al. have used the method with the higher index tellurium oxide (TeO_2) glass and silicon waveguides [7,11]. In Ref. [6], our group used the micro-trench technique with chalcogenide glasses to demonstrate a proof-of-concept for the fabrication of microresonators using solid-state dewetting. The microresonator reported in Ref. [6] had a quality factor of 6×10^5. Recently, we used the micro-trench method with tantalum pentoxide to achieve microresonators with broadband thermal stability [12]. The microresonators in Ref. [12] exhibit a low temperature dependent wavelength shift (TDWS) of 10 pm/K or less over a bandwidth of 120 nm. An overview of the literature is presented in Table 1 to highlight the different materials that have been demonstrated.

Table 1. Review of micro-trench resonator demonstrations

Material	Platform	Application	Refractive index	Ref.
Er/Yb:Al_2O_3	SNOI[a]	Laser	$n = 1.65$	[9]
Tm:Al_2O_3	SNOI	Laser	$n = 1.65$	[10]
TeO_2	SOI[b]	Sensor	$n = 2.05$	[11]
Al_2O_3	SNOI	Passive MR	$n = 1.65$	[13]
TeO_2	SOI	Passive MR	$n = 2.05$	[7]
Ta_2O_5	SOI	Passive MR	$n = 2.07$	[12] and this work
$As_{20}S_{80}$	SOI	Passive MR	$n = 2.19$	[6] and this work
As_2S_3	SOI	Passive MR	$n = 2.42$	[14] and this work
$As_{20}Se_{80}$	SOI	Passive MR	$n = 2.57$	This work
$Ge_{23}Sb_7S_{70}$	SOI	Passive MR	$n = 2.17$	This work

[a]SNOI: Silicon nitride-on-insulator,
[b]SOI: Silicon-on-insulator

In this work, we propose and demonstrate that micro-trench resonators can be used as a universal integration method for amorphous thin films. Our methodology combines numerical simulations of the optical properties of realistic structures and experimental demonstrations that outlines the versatility of the method. Simulations are first used to explore the achievable range of material combination that is compatible with standard 220 nm silicon waveguides. The integration density limit is also considered numerically through the bending leakage limited quality factors. We experimentally demonstrate a variety of materials as well as novel ultra-compact microresonators (MR) with a radius of only 5 μm that exhibit large quality factors over 1.8×10^5. Finally, we present a proof-of-concept multilayer waveguide combining tantalum pentoxide with chalcogenide films to form a composite cross-section.
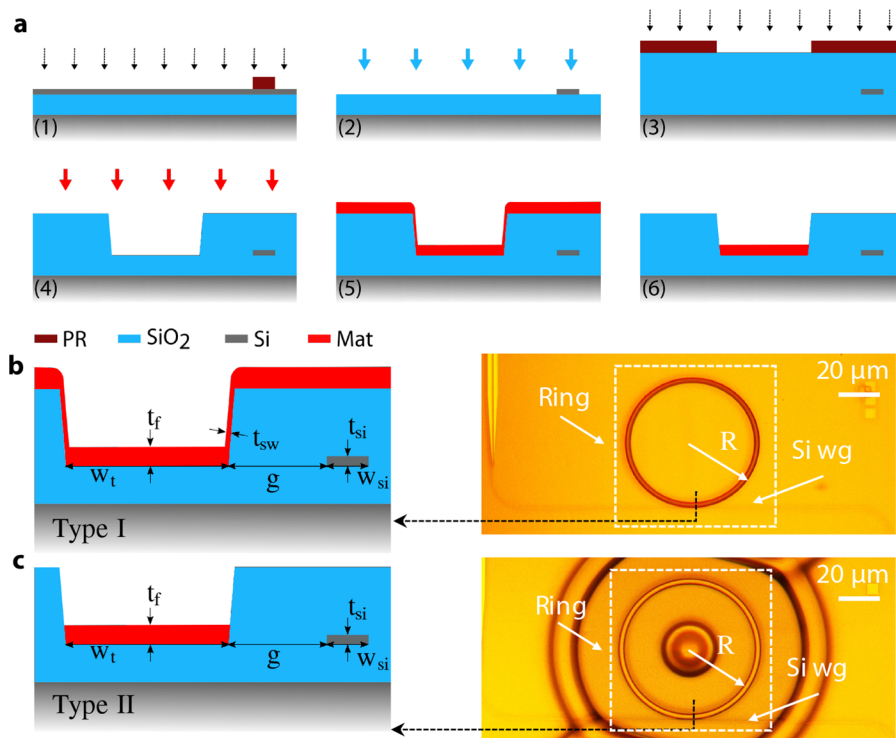
Fig. 1. (a) Schematic of the process flow for the fabrication of micro-trench waveguides co-integrated with silicon waveguides. The steps are as follows: (1) Lithography and etching of the silicon structures, (2) deposition of the top silica cladding, (3) lithography and etching of the micro-trench, (4) thin film deposition, (5) optional process to remove the top layer and leave a rectangular waveguide as shown in (6). In this work, when there is a step (5), it consists of thermal dewetting. (b,c) type I/II waveguide schematic (left) and top view micrograph of a fabricated device (right). The silicon waveguide (Si wg) on the micrographs is faintly visible through the chalcogenide cladding. The materials are identified using different colors: brown for photoresist (PR), light blue for silicon dioxide (SiO_2), grey for silicon (Si) and red for the material to co-integrate (Mat).

2. Methods

In this section, we describe the experimental methods that were used throughout this study. Mainly, we explain how the devices were fabricated, both the bare silicon chips and the micro-trench resonators. To demonstrate versatility, a range of materials with different refractive index and interesting optical properties were chosen. Among them, we opted for multiple chalcogenide glasses as they provide interesting optical properties [15] and their composition is extremely flexible [16,17]. We also explore the use of tantalum pentoxide (Ta_2O_5) for its exceptional nonlinear properties and potential use for lasers and amplifiers [18,19].

2.1. Thin film deposition

In order to deposit chalcogenide thin films, bulk glasses were prepared via the melt-quenching technique using high purity starting materials. Thin films were then deposited using an electron-beam evaporator and a deposition rate of 10 Aring; was chosen for its optimal results. Ta_2O_5 thin films, on the other hand, were prepared using dual magnetron mid-frequency AC reactive sputtering: a pure metallic Ta target, an O_2 flow of 29 cm, and a deposition rate of 4.5

Aring; were used in the process. $As_{20}S_{80}$, $As_{40}S_{60}$, $As_{20}Se_{80}$, and $Ge_{23}Sb_7S_{70}$ chalcogenide glass compositions were selected because they present a large thermal stability $\Delta T = T_x - T_g$ (where T_x and T_g represents the first crystallization temperature and glass transition temperature, respectively) or a non-existent crystallization temperature, and/or a low viscosity when heated above T_g. When those conditions are met, thin films have a high tendency to reflow under heat and dewet from the surface. It is especially the case for chalcogenide glasses [20–22]. For the chalcogenide devices, a 50 nm thick SiO_2 film was deposited by electron-beam evaporation as the last step to prevent surface oxidation.

By dewetting from the SiO_2 substrate, thin films will not only greatly reduce their surface roughness [21,22], but will also better fill the trenches in which they are deposited and reduce small defects or gaps present on the surface [6,23]. In order to obtain such material reflow, one needs to anneal thin films well above the glass transition temperature (T_g). In one of our previous work, thin films of $As_{20}S_{80}$ were thermally treated at $240°$ C for 120 s which corresponds to $T_g + 140°$ C [6]. Colmenares *et al.* described the dewetting of $As_{20}Se_{80}$ thin films for temperatures ranging from $T_g + 80°$ C to $T_g + 150°$ C [21]. For $As_{40}S_{60}$, thermal reflow has already been reported in the literature and is quite well-known [22]. $Ge_{23}Sb_7S_{70}$, on the other hand, does not seem to have been studied extensively regarding thermal reflow/dewetting. The choice of studying this composition relied on its high chalcogen content (Sulfur: 70 at.%), and its relatively low T_g ($311°$ C) and absence of crystallization peak [24]. The dewetting – or thermal reflow – step is realised in a rapid thermal annealing (RTA) oven, at a heating rate of $100°$ C in an inert atmosphere (Ar/N_2).

2.2. Fabrication

The base SOI chips were processed using photolithography by Advanced MicroFoundry (AMF) through a CMC Microsystems supported multiproject wafer (MPW) run. For all devices, the silicon thickness is 220 nm and the buried oxide layer (BOx) is 2 μm thick. The fabrication process flow is presented in Fig. 1(a). Steps 1 to 4 inclusively can be done in standard CMOS photonic foundries (AMF in this case). In its simplest form, the method requires a single back-end step (5) of thin film deposition. In this case, the material will completely cover the chip, forming the geometry shown in Fig. 1(b). A major drawback of this geometry, as will be shown in the next section, is the additional bending loss in curved waveguides. An approach to solve this issue is to use materials that can undergo dewetting (see sect. 2.1) such as chalcogenides. This process breaks the thin films and results in a conformal waveguide in the micro-trench with no sidewall to allow leakage. The issue could also be solved by a chemical-mechanical polishing step following the thin film deposition or a lift-off technique [25,26]. The resulting ideal waveguide is shown in Fig. 1(c) where the retraction of the film following dewetting and the difference with the as-deposited device is obvious from the top view micrographs. For the sake of clarity, the structures shown in Fig. 1(b) and (c) will be referred to as type I and type II waveguides, respectively.

Before the post-process deposition and in the interest of achieving high quality thin films, silicon chips must undergo two pre-processes: (1) a slight wet etching of the SiO_2 cladding to smooth the surface, and (2) a cleaning of any residual material. The first step consists in dipping samples in buffered oxide etchant (BOE: HF/NH_4F) for 5 s. Then, a quenching step in ultrapure water (UPW) is necessary to stop any further etching from the BOE. After that, each sample is set on a spin-coating device and thoroughly cleaned using three solvents: (1) ultrapure water (UPW), (2) acetone, and (3) isopropanol. Any residual humidity is then dried in the oven for $\sim$ 30 min.

2.3. Optical characterization

All the fabricated chips were characterized using a laser swept method. The light was coupled to and from the chips using 100 μm long inverse nanotapers edge couplers with tips width of 180

nm. On-chip routing is done with rib waveguides to mitigate loss and backscattering. Near the coupling region of the MRs, the rib waveguides are converted into strip waveguides for coupling using 40 μm long linear tapers. A polarization paddle was used to control the polarization state at the chip input. Unless stated otherwise, all the measurements were realized with transverse electric (TE) polarized light. The chip stage used a Peltier module and a temperature controller (TEC) to keep the chip temperature fixed at 20° C. The temperature dependence was investigated for certain devices (see sect. 4.3) by varying the temperature of the TEC.

3.   Design

In this section, we present simulations of the basic guiding properties of the micro-trench geometries. All the simulations are done using a commercial finite difference eigenmode solver (FDE) and for operation at λ = 1550 nm, unless stated otherwise. The dimensions of the geometry are summarized in Fig. 1(b) and (c). The sidewall angle is fixed at $\theta = 7°$, according to the angle measured in fabricated devices. The thickness of the sidewall materials t_{sw} is fixed to half the deposited thickness. The thickness of the top cladding is 3 μm.

3.1.   Modal analysis

Fig. 2(a) shows the simulated effective index of the supported modes in a 2 μm wide and 1 μm thick straight type II waveguide for both polarizations (quasi-TE and quasi-TM), the refractive index of the core is varied from n = 1.65 to n = 2.45. An important takeaway from this data is that micro-trench waveguides are almost always multimodes. In fact, the dimensions applied here represent well the physical limitations of the fabrication. The top silica cladding of SOI chips is usually between 2 μm and 3 μm thick. In order for modes to be well guided in type I waveguides, the thickness of the core must be significantly smaller than the thickness of the cladding. Although this requirement is relaxed for type II waveguides, the core thickness is still limited to being lower than the cladding. The deep trenches that need to be etched to reach the level of the silicon device (2-3 μm) are challenging and results in significantly slanted sidewalls because of the angle. This in turn puts a limitation on the width of the micro-trench. In fact, using the AMF fabrication process, the design rules prohibit $w_t < 2.0$ μm. This justifies our choice of the width for most of this work. Therefore, most relevant materials will result in multimode operation when used for the core of micro-trench waveguides. From Fig. 2(a), the single mode cutoff is around n = 1.65. Fig. 2(b) presents the effective index of the modes supported in a waveguide with n = 2.05 and t_f = 1.0 μm when varying the width well below the foundry design limit. Even narrower waveguides with a moderate index still supports multiple modes. The single-mode cutoff for the waveguide in Fig. 2(b) is below 1.0 μm. We conclude that micro-trench waveguides are limited to multimode operation. While these restrictions might appear difficult, it is important to keep in mind the simplicity of using streamlined, commercially available CMOS foundries. Furthermore, we note the possibility to engineer the coupling section to selectively excites a target mode [27].

3.2.   Microring resonators

In this section, we are interested in the properties of micro-trench waveguides used to form microring resonators. Most demonstrations of micro-trench integration were based on MRs like those shown in the right panels of Fig. 1(b) and (c). MRs are fully described by their quality factors Q, describing the circulating time of photons in the cavity, and their free-spectral range (FSR), corresponding to the inverse of the round-trip time of photons in the cavity. The static properties of all-pass microring resonators are well established and can be found in various Refs. [28,29]. The total quality factor can be experimentally measured as the ratio of the resonant wavelength λ_r to the full width at half maximum of the resonance *FWHM* such that $Q = \lambda_r / FWHM$. Increasing the quality factor of MRs and, correspondingly, decreasing the propagation loss of waveguides is
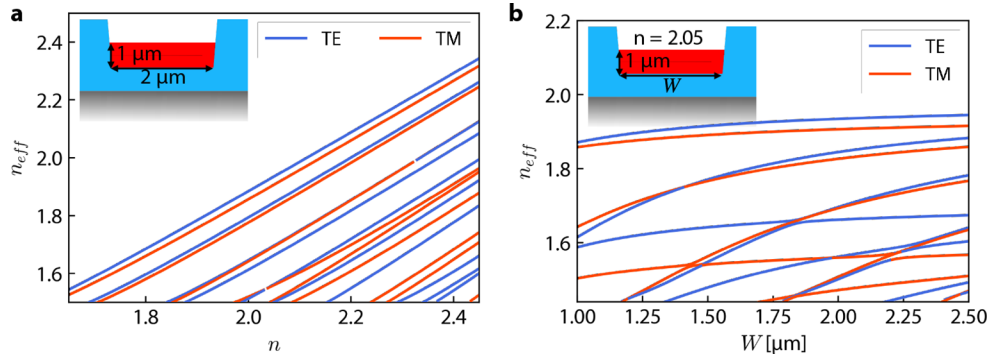
Fig. 2. (a) Effective index of the guided modes in a waveguide with $w_t = 2.0$ μm and $t_f = 1.0$ μm with varying refractive index n. (b) Effective index of the guided modes in a waveguide with a fixed refractive index $n = 2.05$ and $t_f = 1.0$ μm. Both figures consider type II waveguides.

still one of the most important endeavors of integrated photonics [30–33]. From a theoretical perspective, multiple physical mechanism contribute to loss and reduce the value of Q, including coupling to the bus waveguide Q_c, loss from scattering Q_s, material absorption Q_a, loss from bending leakage Q_b and, specific to integrated optics, loss from substrate leakage Q_l. The total Q is then given as

$$Q^{-1} = Q_c^{-1} + Q_s^{-1} + Q_a^{-1} + Q_b^{-1} + Q_l^{-1}. \tag{1}$$

While Q_c^{-1} can be inferred from the coupling condition and the phase response of the MR, differentiating the contribution of scattering, absorption and leakage in experiments can be challenging. Their contributions are often agglomerated into a single intrinsic quality factor $Q_i^{-1} = Q_s^{-1} + Q_a^{-1} + Q_b^{-1} + Q_l^{-1}$. Experimentally, the intrinsic quality-factor can be obtained from the transmittance in the undercoupled regime as [29,34]

$$Q_i = \frac{2Q}{1 + \sqrt{T_0}}, \tag{2}$$

where T_0 is the transmittance at the resonant wavelength. Assuming low round-trip loss and weak coupling, Q_i is directly related to the waveguide propagation loss α as [29]

$$Q_i \approx \frac{2\pi n_g}{\alpha \lambda_r}, \tag{3}$$

with n_g the group index at the resonant wavelength. Therefore, the intrinsic quality factor can be used to infer the propagation loss in the waveguide and compare different devices.

3.3. *Mode leakage*

Here, we numerically consider the leakage loss in micro-trench waveguides. As stated in sect. 1, an ideal heterogeneous integration method should not compromise the high integration density of SOI. The footprint of an MR is dictated by its bending radius, to which the lower bound is fixed by the acceptable bending leakage loss. As the radius is reduced, optical power will radiate out of the core and be lost. The other source of leakage is coupling to the high-index silicon substrate mode that is separated from the waveguide by the BOx layer. A thin BOx or a weakly confined mode will result in additional loss. This puts another limit on the material refractive index and waveguide dimensions. Here the bending loss limited quality factor Q_b and substrate leakage quality factor Q_l are estimated for a variety of materials as the radius and thickness of the

BOx layer are varied. To isolate the bending loss, the BOx thickness is set to ∞ while to isolate the substrate leakage, we simulate a straight waveguide with a finite BOx and a large simulation window width of 25 μm. All the simulations are done with waveguide dimensions $w_t = 2.5$ μm and $t_f = 1.0$ μm.

Figure 3(a) and (b) summarizes the substrate leakage limited quality factor Q_l for type I and type II waveguides, respectively. The BOx thickness is set to common SOI values: 1 μm, 2 μm and 3 μm. Substrate leakage is only problematic for 1 μm as this loss mechanism becomes dominant even for moderate refractive index. For thicker BOx, only the lowest n will experience significant leakage. For the type I waveguide, the maximum Q_l are limited by leakage in the top sections of the waveguides even for straight geometries ($R \to \infty$).
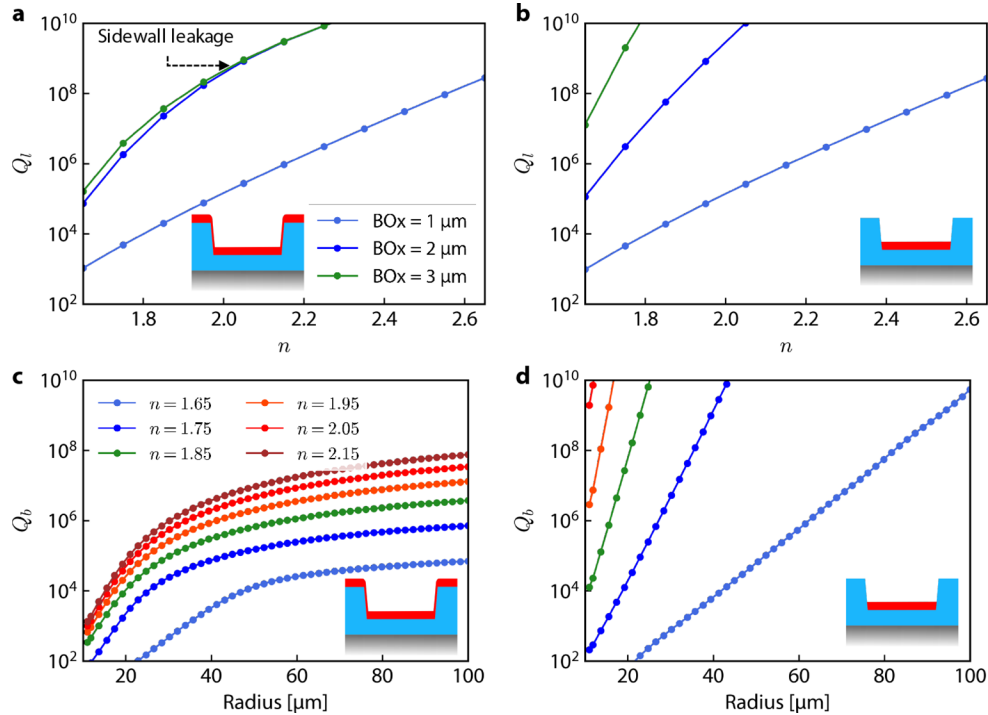

Fig. 3. Simulated quality factor limited by (a,b) substrate leakage Q_l and (c,d) bending leakage Q_b. Type I waveguides are shown in (a) and (c) while type II waveguides are shown in (b) and (d). The waveguide dimensions are constant at $w_t = 2.5$ μm and $t_f = 1.0$ μm.

Figure 3(c) and (d) summarizes the bending loss limited quality factor Q_b for the fundamental TE-mode of type I and type II waveguides, respectively, using various materials with index ranging from $n = 1.65$ to $n = 2.15$. The quality factors of type I waveguides saturate at around $Q_b = 10^8$, which in itself is only problematic for ultra-high Q MRs. For comparison, the record Q_i in a planar integration MR is $Q = 4.22 \times 10^8$ [35]. However, the leakage loss in type I waveguides becomes problematic for compact structures or low-index materials as Q_b rapidly falls below 10^5, a moderate value in contrast with the state-of-the-art. The scattering limited quality factor Q_s is usually the limiting factor in integrated optics, as Q_b can be designed such that $Q_b \gg Q_s$. The advantage of using type II waveguides is obvious from comparing Fig. 3(c) and (d), as they offer extremely high Q_b even for moderate index ($n < 2$) and ultra-compact MRs with $R < 10$ μm. This drastically different behavior is understood from the absence of a leakage channel in the waveguide sidewalls (see Fig. 1(b) and (c)). These results suggest that the method does not compromise the integration density of SOI unless low index materials $n < 1.85$ are used

in conjunction with a small radius. We note that high-Q MRs ($Q_i > 1 \times 10^6$) with low-index (Al$_2$O$_3$, n= 1.65) type I waveguides were achieved with thicker SiO$_2$ cladding (5 μm) and an additional silicon nitride waveguide next to the micro-trench to increase the guiding strength [13].

3.4. *Phase matching*

Power transfer between the highly dissimilar silicon bus waveguide and the micro-trench waveguide is non-trivial. The approach used for the experimental demonstration in this work is based on point coupling, where the bus waveguide is kept straight and brought in close proximity to the microresonator. We consider the phase mismatch $\Delta\beta = \frac{2\pi}{\lambda}(n_{\text{eff,ring}} - n_{\text{eff,bus}})$ in the context of using materials with various refractive index. A large phase mismatch will limit the maximum power transfer between the waveguides [36]. For high-Q MRs, it is possible to achieve critical coupling even with significant phase mismatch. However, achieving strong overcoupling can be limited by a non-zero phase mismatch. We focus on the range of materials that could be integrated considering the silicon waveguide effective index. Extended design and optimization are left for future work.

Fig. 4 compares the effective index of the silicon bus waveguide with a variety of type II waveguides. The index are chosen to sample interesting materials (see. Table 1). The first thing to notice is that by varying the width of the silicon waveguide, it is possible to achieve phase matching ($\Delta\beta = 0$) with a large variety of materials and waveguide dimensions. This speaks of the flexibility of the integration approach. The silicon/silica core/cladding system offers a larger freedom for phase matching in contrast with other possibilities, such as the silicon nitride/silica combination. This is because the achievable effective index is bounded as $n_{clad} > n_{eff} > n_{core}$. The effective index is controlled by varying the transerval dimensions of the waveguide. Because of the large difference between n_{SiO_2} and n_{Si}, the range of material index that can be phase-matched is broad.
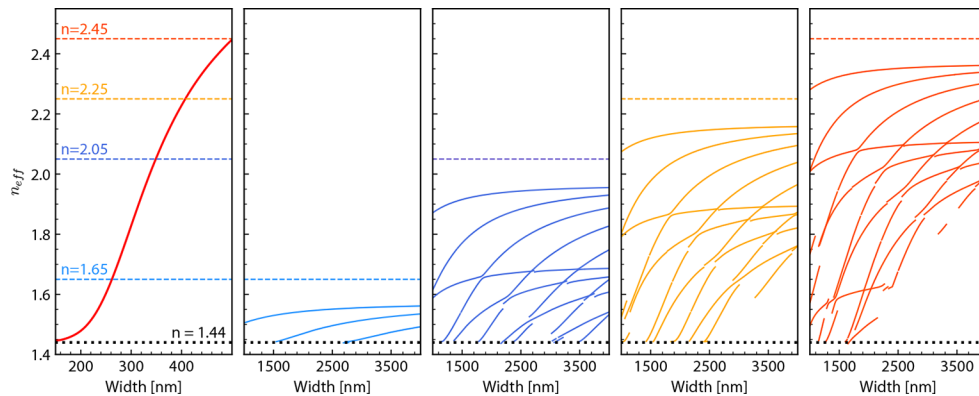

Fig. 4. Effective index of (left panel) the fundamental quasi-TE mode in a 220 nm thick silicon waveguide with varying width and of (right panels) the guided (up to 20) quasi-TE modes in type II waveguides with $t_f = 1$ μm, varying width and different refractive index: from left to right, $n = 1.65$, $n = 2.05$, $n = 2.25$, $n = 2.45$.

We also note that the simulations in Fig. 4 are limited to $n_{eff} = 2.45$ since this is about the limit where the silicon waveguide is single-mode. Operating the silicon waveguide in the multimode regime is possible but requires careful design to excite only the target mode in the bus waveguide, for example by using adiabatic tapers. Nevertheless, having a multimode bus waveguide is generally not optimal as it can reduce the coupling ideality, an important figure of merit for microresonators used in nonlinear optics and quantum optics applications [37]. We also note that it is possible to couple light from a silicon waveguide with a lower effective index than the

fundamental mode of the ring waveguide. In this case, higher order modes will be excited in the ring. The coupling section can be designed such that a given mode is selectively excited [27].

4. Experimental results

4.1. Material diversity

In this section, we present selected experimental results of micro-trench MRs with various materials. Multiple hybrid MRs were fabricated and tested using the methods highlighted in sect. 2.3 to experimentally confirm the versatility of the technique. The intrinsic quality factors and waveguide propagation loss were calculated using the methods presented in sect. 3.2.

Scanning electron microscope (SEM) images of MRs are shown in Fig. 5. The leftmost panels show cross-sections that were obtained by focused ion beam (FIB) milling in (a) and by cleaving the chip in (d). Fig. 5(a) is an example of a type I waveguide, where the deposited material on the sidewalls and on the cladding top can act as leakage channels (see sect. 3). On the other hand, Fig. 5(d) shows a type II waveguide that was achieved using a dewetting step which left no visible material on the sidewalls. We note that FIB was not used on the chalcogenide structures to prevent evaporating the glass. Fig. 5(b), (c), (e) and (f) show perspective SEM images of various materials microresonators with type I waveguides in (b,c) and type II waveguides in (e,f). Fig. 5(e) is a good example of very aggressive dewetting that was obtained using a well-optimized process (240° C for 120 s.). The dewetting of $As_{20}S_{80}$ was studied in more details in Ref. [6]. On the other hand, Fig. 5(f) shows an $As_{20}Se_{80}$ MR with very soft dewetting and barely any rim retraction. While the dewetting of $As_{20}Se_{80}$ is well studied [21,38], its use in templated structures such as those presented here is new. The parameters for the dewetting of $As_{20}Se_{80}$ (180° C for 120 s) were chosen heuristically. The chip with $Ge_{23}Sb_7S_{70}$ underwent annealing at 400° C for 300 s in an effort to reduce the surface roughness of the film.
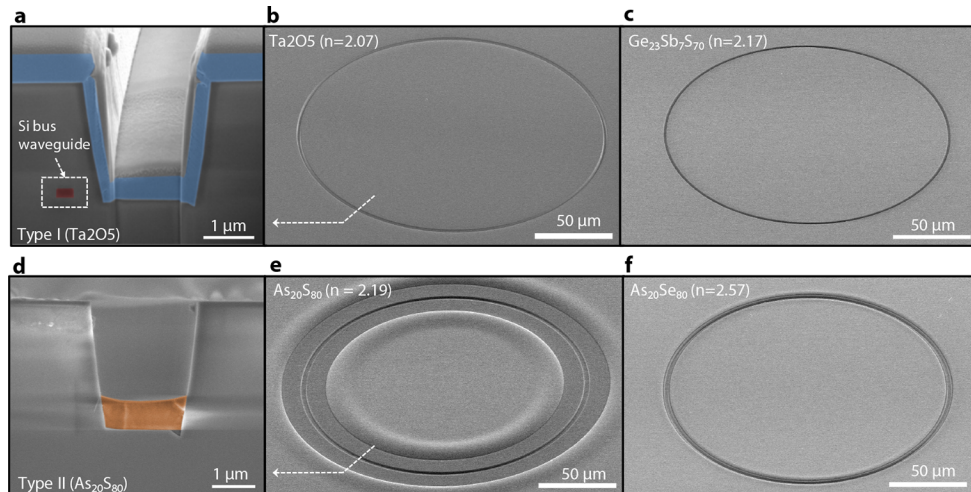

Fig. 5. Cross-section SEM images of a (a) type I waveguide and (d) type II waveguide. (b,c,e,f) Perspective SEM images of MRs with $R = 100$ μm using different thin film materials with refractive index: (b) Ta_2O_5, $n = 2.07$ (c) $Ge_{23}Sb_7S_{70}$ $n = 2.17$, (e) $As_{20}S_{80}$ $n = 2.19$ and (f) $As_{20}Se_{80} = 2.57$. (b) and (c) are examples of type I waveguides while (e) and (f) are examples of type II waveguides.

Finally, the transmittance of selected MRs with $R = 100$ μm are presented in Fig. 6. The corresponding FSRs are shown directly on the figure and varies between 1.47 nm for $As_{40}S_{60}$ and 1.77 nm for $Ge_{23}Sb_7S_{70}$. The small differences between the FSRs are due to effective index

and dispersion difference between the waveguides. The group index are $n_g = 2.28$ for Ta_2O_5, $n_g = 2.32$ for $Ge_{23}Sb_7S_{70}$, $n_g = 2.58$ for $As_{40}S_{60}$ and $n_g = 2.32$ for $As_{20}S_{80}$. The intrinsic quality factors also vary between the different materials from below 5×10^4 for Ta_2O_5 to roughly 1×10^6 for $As_{20}S_{80}$. The intrinsic quality factor of the MRs with $Ge_{23}Sb_7S_{70}$ and $As_{40}S_{60}$ are about 6×10^4 and 2.3×10^5, respectively.
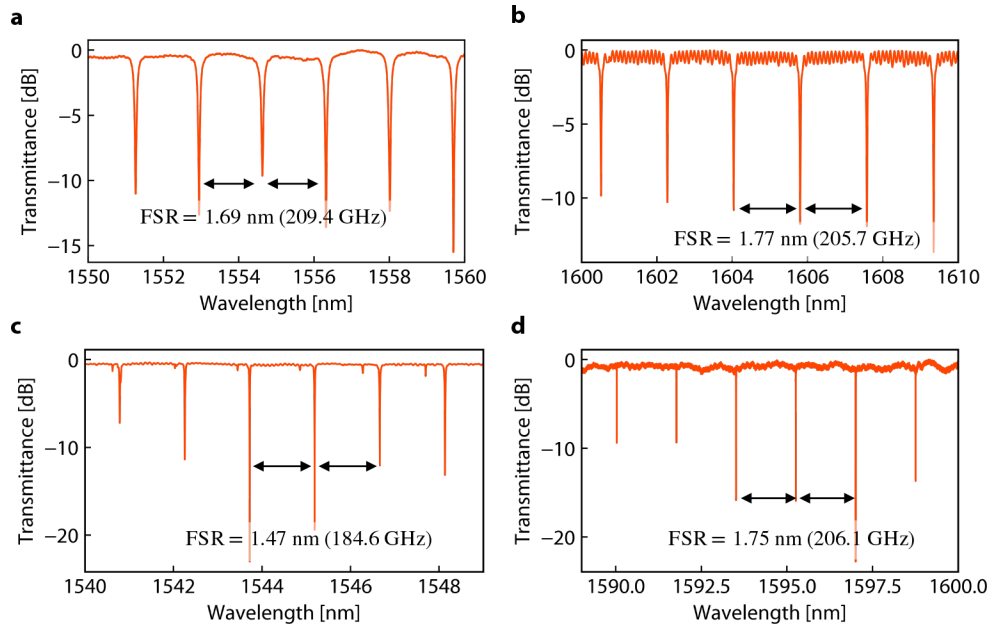

Fig. 6. Measured transmittance of micro-trench resonators with $R = 100$ μm and various materials (a) Type I and Ta_2O_5, (b) Type I and $Ge_{23}Sb_7S_{70}$, (c) Type II and $As_{40}S_{60}$ and (d) Type II and $As_{20}S_{80}$.

It is important to comment on the significant difference between the quality factors of the fabricated devices. According to simulations, the difference is unlikely to arise from bending leakage (see Fig. 3(c) and (d)). Roughness scattering is also unlikely the determining factor, mainly because the trend is the opposite of what would be expected, i.e., higher index contrast should lead to increases loss, not the opposite [39]. We also emphasize that the sidewall roughness comes from the silicon dioxide micro-trench etch, which is the same for all devices. Therefore, the large loss discrepancy between the fabricated devices is attributed to the background loss of the material thin films. We note that $As_{20}S_{80}$ and $As_{40}S_{60}$ depositions were optimized in previous works [6,14]. We found that the dewetting helps achieve smooth and conformal waveguides, which reduces the scattering loss from the thin film surface. SEM images of the $Ge_{23}Sb_7S_{70}$ film (not shown here) indicated high surface roughness, even after annealing, which partially explains the low quality factors observed. Standard microring resonators using Ge-Sb-S glass were previously demonstrated with $Q>1 \times 10^6$ [40], suggesting that much higher Q could be achieved with the micro-trench geometry and an optimized film deposition technique.

Higher-order modes only appear in the spectra of Fig. 6(c), indicating that a certain degree of mode selectivity was achieved. The $As_{40}S_{60}$ MR in (c) was annealed at 300° C for 120 s. to induce a moderate dewetting. The silicon waveguide widths for the MRs presented in Fig. 6 are (a) $w_{Si} = 315$ nm, (b) $w_{Si} = 360$ nm, (c) $w_{Si} = 400$ nm and (d) $w_{Si} = 400$ nm. Even if the coupling for each material was not carefully optimized, satisfactory coupling with near critical condition (extinction ratio >20 dB) was achieved.

4.2.   Ultra-compact chalcogenide microresonator

Here, we present the results of chalcognide MRs with bend radius comparable to silicon MRs to demonstrate that the micro-trench filling approach can enable satisfactory integration density. Two MRs with radius of $R = 5$ μm were fabricated and characterized, one with $As_{20}S_{80}$ ($n = 2.19$) and one with $As_{20}Se_{80}$ ($n = 2.57$). MRs with large radius $R > 100$ μm were demonstrated in the previous section and were used exclusively in previous work regarding micro-trench resonators [6,7,9–11,13,14]. Yet, Fig. 3 shows that it should be possible to achieve very compact structures when combining high-index materials with type II waveguides. Such structures are possible with dewetted chalcogenide thin films. The results are summarized in Fig. 7, which shows micrographs of the fabricated devices, the measured transmittances and the relatively high quality factors achieved. The $As_{20}S_{80}$ and $As_{20}Se_{80}$ MRs dimensions are $w_t = 2.5$ μm, $t_f = 1.0$ μm and $w_t = 2.5$ μm, $t_f = 0.65$ μm, respectively. The FSR is indicated on each plot and the corresponding group index are $n_g = 2.57$ and $n_g = 3.12$.

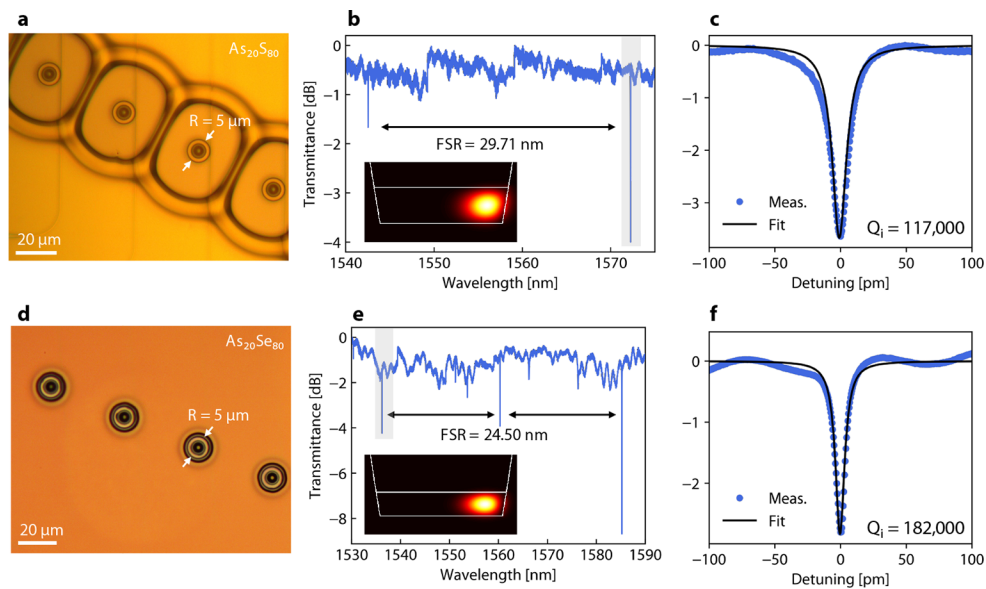**Fig. 7.** (a,d) Top view micrograph of $As_{20}S_{80}$ and $As_{20}Se_{80}$ MR with $R = 5$ μm, respectively. (b,c) Measured transmittances with an inset showing the simulated electric field intensity mode profile at 1550 nm. (c,f) Single resonance with a Lorentzian fit to extract Q.

For both MRs, the Q_i is well over 1×10^5, suggesting moderate loss even with tight bends. The corresponding propagation loss estimated using Eq. (3) are $\alpha = 3.9$ dB/cm and $\alpha = 3.0$ dB/cm for the $As_{20}S_{80}$ and $As_{20}Se_{80}$ MR, respectively. The small difference in loss could be attributed to the tighter confinement in $As_{20}Se_{80}$ due to the higher index. We note that the wavelength difference between the measurements could also affect the measured loss. The extracted propagation loss are comparable with silicon microring resonators of the same radius [41]. In both cases, increasing the radius resulted in improved quality factors (not shown), suggesting that bending leakage is the dominant source of loss. Nevertheless, the high Qs indicates that even with bending leakage, these MRs have satisfactory loss for certain applications and compares favorably with other demonstrations of ultracompact MRs [42]. These results confirm that the heterogeneous integration method proposed in this work comes at a very small or negligible density cost.

4.3. Multi-layer waveguides

The geometry and fabrication process of micro-trench waveguides are favorable to heterogeneous multilayered cross-sections, where different materials are vertically stacked by subsequent depositions. This type of waveguide could find applications in dispersion engineering or athermal photonics [43,44]. Yet, the use of such waveguides has remained limited to theoretical investigations, in part because of the fabrication complexity. In this section, we present a novel multilayer MR based on the micro-trench geometry. We fabricated an MR with $R = 100$ μm by subsequently depositing an 800 nm Ta_2O_5 base layer, a 200 nm $As_{20}S_{80}$ layer and a final 50 nm SiO_2 passivation layer. The deposition methods are described in sect. 2.

The multilayer waveguide is schematically depicted in Fig. 8(a) and its optical properties are summarized in (b) through (e). The intrinsic quality factors are slightly over $Q_i > 6 \times 10^4$ for the bandwidth considered. We observe anomalous dispersion with a disturbance near 1565 nm due to higher-order modes. This disturbance is visible in Fig. 8(d) where the insets (i) and (ii) show a disturbed resonance and a normal resonance, respectively. Finally, the temperature dependent wavelength shift $TDWS = d\lambda/dT$ was measured and shown in Fig. 8(e). The negative $TDWS$ is due to the negative thermo-optic coefficient TOC of the chalcogenide [45] and suggest that the weak TOC of Ta_2O_5 is overcompensated by the thin film of chalcogenide [46]. While this demonstration is meant as a proof-of-concept, it highlights well the versatility and the universality of the micro-trench filling approach for heterogeneous integration with silicon waveguides.
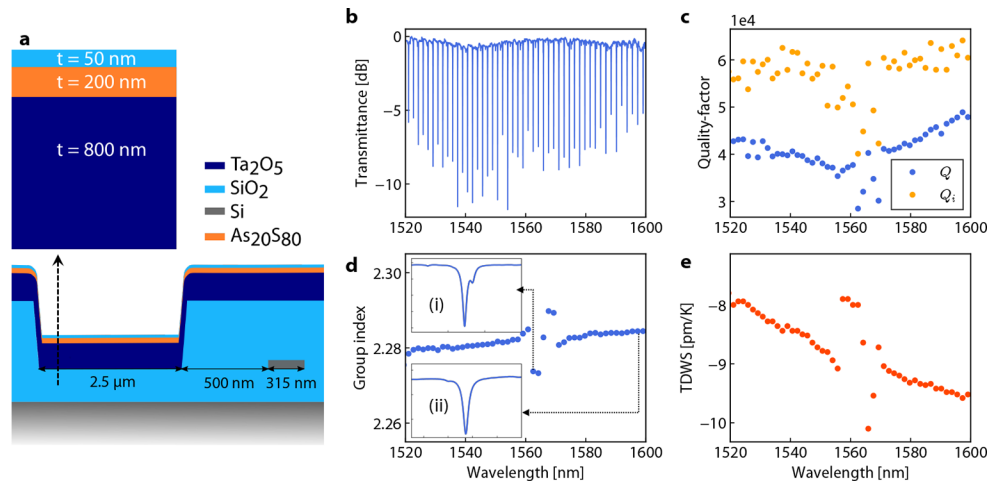

Fig. 8. (a) Schematic of the multilayer waveguide combining Ta_2O_5 and $As_{20}S_{80}$. (b) Measured transmittance, (c) quality factor (d) group index and (e) temperature dependent wavelength shift $TDWS$ of the multilayer with $R = 100$ μm. The insets in (d) show a perturbed resonance (i) and an unperturbed resonance (ii).

5. Discussion

At this point, comparison with similar methods of co-integration can be instructive. In fact, the keen reader might ask what is the advantage of using a micro-trench filling method versus defining the waveguides directly in the advanced material. It is true that such an approach has been used to great success, for example with chalcogenides waveguides [47,48]. The main appeal of micro-trench filling is its universality, as the fabrication method is readily compatible with various materials that would require dedicated, sometimes tricky, etching recipes if developed individually. Furthermore, materials like chalcogenides are not part of the standard CMOS process, therefore, they should be restricted to a wafer-scale, backend process, as it is possible to

do with micro-trench filling. We believed that these advantages make up for the design restrictions inherent to the method.

Another aspect to emphasize about the method is its use with active materials. The addition of rare-earth ions inside the thin film can result in difficulty to achieve a good quality waveguide etch and increase background propagation loss [49]. By not requiring direct etch of the material, micro-trench filling effectively bypass this problem. Moreover, for large-scale integration, it is preferable to not have all circuits made from the active material as the pump wavelength would be absorbed in the routing sections. Micro-trench filling then allows the seamless integration of active components into otherwise passive circuitry. In fact, the first reports using this approach were demonstrations of rare-earth doped microlasers on silicon nitride [9,10].

6. Conclusion

In summary, we presented in-depth simulations of micro-trench resonators coupled to silicon waveguides and showed that the geometry that accommodate a large variety of materials, making it an interesting candidate for universal heterogeneous integration. We fabricated and tested microresonators with various thin film materials to further reinforce this point. We reported novel structures using this method, including ultra-compact and high-Q microresonators as well as multilayered waveguides that have potential for dispersion engineering and athermal photonics.

Disclosures. The authors declare no conflicts of interest.

Data availability. Data underlying the results presented in this paper are not publicly available at this time but may be obtained from the authors upon reasonable request.

References

1. S. Chung, H. Abediasl, and H. Hashemi, "15.4 a 1024-element scalable optical phased array in 0.18μm SOI CMOS," in *2017 IEEE International Solid-State Circuits Conference (ISSCC)*, (2017), pp. 262–263.
2. M. Zhang, C. Wang, P. Kharel, D. Zhu, and M. Lončar, "Integrated lithium niobate electro-optic modulators: when performance meets scalability," Optica **8**(5), 652–667 (2021).
3. D. J. Moss, R. Morandotti, A. L. Gaeta, and M. Lipson, "New cmos-compatible platforms based on silicon nitride and hydex for nonlinear optics," Nat. Photonics **7**(8), 597–607 (2013).
4. W. Shi, Y. Tian, and A. Gervais, "Scaling capacity of fiber-optic transmission systems via silicon photonics," Nanophotonics **9**(16), 4629–4663 (2020).
5. L. Chrostowski, H. Shoman, M. Hammood, H. Yun, J. Jhoja, E. Luan, S. Lin, A. Mistry, D. Witt, N. A. F. Jaeger, S. Shekhar, H. Jayatilleka, P. Jean, S. B.-d. Villers, J. Cauchon, W. Shi, C. Horvath, J. N. Westwood-Bachman, K. Setzer, M. Aktary, N. S. Patrick, R. J. Bojko, A. Khavasi, X. Wang, T. Ferreira de Lima, A. N. Tait, P. R. Prucnal, D. E. Hagan, D. Stevanovic, and A. P. Knights, "Silicon photonic circuit design using rapid prototyping foundry process design kits," IEEE J. Sel. Top. Quantum Electron. **25**(5), 1–26 (2019).
6. P. Jean, A. Douaud, V. Michaud-Belleau, S. H. Messaddeq, J. Genest, S. LaRochelle, Y. Messaddeq, and W. Shi, "Etchless chalcogenide microresonators monolithically coupled to silicon photonic waveguides," Opt. Lett. **45**(10), 2830–2833 (2020).
7. H. C. Frankis, D. B. Bonneville, and J. D. B. Bradley, "Tellurite glass microcavity resonators integrated on a silicon photonics platform," J. Opt. Microsystems **1**(02), 1–12 (2021).
8. M. Xin, N. Li, N. Singh, A. Ruocco, Z. Su, E. S. Magden, J. Notaros, D. Vermeulen, E. P. Ippen, M. R. Watts, and F. X. Kärtner, "Optical frequency synthesizer with an integrated erbium tunable laser," Light: Sci. Appl. **8**(1), 122 (2019).
9. J. D. B. Bradley and E. S. Hosseini, "Monolithic erbium- and ytterbium-doped microring lasers on silicon chips," Opt. Express **22**(10), 12226–12237 (2014).
10. Z. Su, N. Li, E. S. Magden, M. Byrd, Purnawirman, T. N. Adam, G. Leake, D. Coolbaugh, J. D. B. Bradley, and M. R. Watts, "Ultra-compact and low-threshold thulium microcavity laser monolithically integrated on silicon," Opt. Lett. **41**(24), 5708–5711 (2016).
11. H. C. Frankis, D. Su, D. B. Bonneville, and J. D. B. Bradley, "A tellurium oxide microcavity resonator sensor integrated on-chip with a silicon waveguide," Sensors **18**(11), 4061 (2018).
12. P. Jean, A. Douaud, S. T. Bah, S. LaRochelle, Y. Messaddeq, and W. Shi, "Silicon-coupled tantalum pentoxide microresonators with broadband low thermo-optic coefficient," Opt. Lett. **46**(15), 3813–3816 (2021).

13. Z. Su, N. Li, H. C. Frankis, E. S. Magden, T. N. Adam, G. Leake, D. Coolbaugh, J. D. B. Bradley, and M. R. Watts, "High-q-factor al2o3 micro-trench cavities integrated with silicon nitride waveguides on silicon," Opt. Express **26**(9), 11161–11170 (2018).

14. P. Jean, A. Douaud, S. LaRochelle, Y. Messaddeq, and W. Shi, "Hybrid integration of high-q chalcogenide microring resonators on silicon-on-insulator," in *Conference on Lasers and Electro-Optics*, (Optical Society of America, 2020), p. STh3O.3.

15. B. J. Eggleton, B. Luther-Davies, and K. Richardson, "Chalcogenide photonics," Nat. Photonics **5**(3), 141–148 (2011).

16. Y. Wang, S. Qi, Z. Yang, R. Wang, A. Yang, and P. Lucas, "Composition dependences of refractive index and thermo-optic coefficient in ge-as-se chalcogenide glasses," J. Non-Cryst. Solids **459**, 88–93 (2017).

17. I. Shpak, I. Rosola, and O. I. Shepak, "Temperature dependence of the refractive index of glassy alloys of the As_xS_{100-x} System," J. Appl. Spectrosc. **84**(1), 140–143 (2017).

18. H. Jung, S.-P. Yu, D. R. Carlson, T. E. Drake, T. C. Briles, and S. B. Papp, "Tantala kerr nonlinear integrated photonics," Optica **8**(6), 811–817 (2021).

19. A. Z. Subramanian, G. S. Murugan, M. N. Zervas, and J. S. Wilkinson, "Spectroscopy, modeling, and performance of erbium-doped ta_2o_5 waveguide amplifiers," J. Lightwave Technol. **30**(10), 1455–1462 (2012).

20. A. Douaud, S. H. Messaddeq, and Y. Messaddeq, "Microstructure formation in chalcogenide thin films assisted by thermal dewetting," J. Mater. Sci.: Mater. Electron. **28**(10), 6989–6999 (2017).

21. Y. N. Colmenares, S. H. Messaddeq, and Y. Messaddeq, "Studying the kinetics of microstructure formation through dewetting of As-Se thin films," Phys. Rev. Mater. **5**(1), 015605 (2021).

22. J. Hu, N.-N. Feng, N. Carlie, L. Petit, A. Agarwal, K. Richardson, and L. Kimerling, "Optical loss reduction in high-index-contrast chalcogenide glass waveguides via thermal reflow," Opt. Express **18**(2), 1469–1478 (2010).

23. P. Jean, A. Douaud, S. LaRochelle, Y. Messaddeq, and W. Shi, "Silicon subwavelength grating waveguides with high-index chalcogenide glass cladding," Opt. Express **29**(13), 20851–20862 (2021).

24. C. Smith, J. Jackson, L. Petit, C. Rivero-Baleine, and K. Richardson, "Processing and characterization of new oxy-sulfo-telluride glasses in the ge–sb–te–s–o system," J. Solid State Chem. **183**(8), 1891–1899 (2010).

25. M. H. P. Pfeiffer, A. Kordts, V. Brasch, M. Zervas, M. Geiselmann, J. D. Jost, and T. J. Kippenberg, "Photonic damascene process for integrated high-q microresonator based nonlinear photonics," Optica **3**(1), 20–25 (2016).

26. J. Hu, V. Tarasov, N. Carlie, N.-N. Feng, L. Petit, A. Agarwal, K. Richardson, and L. Kimerling, "Si-cmos-compatible lift-off fabrication of low-loss planar chalcogenide waveguides," Opt. Express **15**(19), 11798–11807 (2007).

27. E. S. Hosseini, S. Yegnanarayanan, A. H. Atabaki, M. Soltani, and A. Adibi, "Systematic design and fabrication of high-q single-mode pulley-coupled planar silicon nitride microdisk resonators at visible wavelengths," Opt. Express **18**(3), 2127–2136 (2010).

28. W. Bogaerts, P. de Heyn, T. van Vaerenbergh, K. de Vos, S. Kumar Selvaraja, T. Claes, P. Dumon, P. Bienstman, D. van Thourhout, and R. Baets, "Silicon microring resonators," Laser Photonics Rev. **6**(1), 47–73 (2012).

29. P. Rabiei, W. H. Steier, C. Zhang, and L. R. Dalton, "Polymer micro-ring filters and modulators," J. Lightwave Technol. **20**(11), 1968–1975 (2002).

30. A. Biberman, M. J. Shaw, E. Timurdogan, J. B. Wright, and M. R. Watts, "Ultralow-loss silicon ring resonators," Opt. Lett. **37**(20), 4236–4238 (2012).

31. M. Zhang, C. Wang, R. Cheng, A. Shams-Ansari, and M. Lončar, "Monolithic ultra-high-q lithium niobate microring resonator," Optica **4**(12), 1536–1537 (2017).

32. X. Ji, F. A. S. Barbosa, S. P. Roberts, A. Dutt, J. Cardenas, A. Okawachi, A. Bryant, A. L. Gaeta, and M. Lipson, "Ultra-low-loss on-chip resonators with sub-milliwatt parametric oscillation threshold," Optica **4**(6), 619–624 (2017).

33. J. Liu, G. Huang, R. N. Wang, J. He, A. S. Raja, T. Liu, N. J. Engelsen, and T. J. Kippenberg, "High-yield, wafer-scale fabrication of ultralow-loss, dispersion-engineered silicon nitride photonic circuits," Nat. Commun. **12**(1), 2236 (2021).

34. L. W. Luo, G. S. Wiederhecker, J. Cardenas, and M. Lipson, "High quality factor etchless silicon photonic ring resonators," Opt. Express **19**(7), 6284 (2011).

35. M. W. Puckett, K. Liu, N. Chauhan, Q. Zhao, N. Jin, H. Cheng, J. Wu, R. O. Behunin, P. T. Rakich, K. D. Nelson, and D. J. Blumenthal, "422 million intrinsic quality factor planar integrated all-waveguide resonator with sub-mhz linewidth," Nat. Commun. **12**(1), 934 (2021).

36. A. Yariv and P. Yeh, *Photonics* (Oxford University Press, 2006).

37. M. H. P. Pfeiffer, J. Liu, M. Geiselmann, and T. J. Kippenberg, "Coupling ideality of integrated planar high-*q* microresonators," Phys. Rev. Appl. **7**(2), 024026 (2017).

38. Y. N. Colmenares, W. Correr, S. H. Messaddeq, and Y. Messaddeq, "Controlling thermal-induced dewetting of as20se80 thin films for integrated photonics applications," Opt. Mater. Express **11**(6), 1720–1732 (2021).

39. F. P. Payne and J. P. R. Lacey, "A theoretical analysis of scattering loss from planar optical waveguides," Opt. Quantum Electron. **26**(10), 977–986 (1994).

40. Q. Du, Y. Huang, J. Li, D. Kita, J. Michon, H. Lin, L. Li, S. Novak, K. Richardson, W. Zhang, and J. Hu, "Low-loss photonic device in ge–sb–s chalcogenide glass," Opt. Lett. **41**(13), 3090–3093 (2016).

41. S. Xiao, M. H. Khan, H. Shen, and M. Qi, "Compact silicon microring resonators with ultra-low propagation loss in the c band," Opt. Express **15**(22), 14467–14475 (2007).

42. X. Guan, M. Fu, Y. Zheng, W. Yi, J. Qi, G. Li, S. Yin, and X. Li, "Ultra-compact titanium dioxide micro-ring resonators with sub-10-µm radius for on-chip photonics," Photonics Res. **9**(7), 1416–1422 (2021).

43. L. Xu, Y. Guo, J. Wang, Z. Han, H. Liu, J. Michel, L. C. Kimerling, and L. Zhang, "Broadband athermal waveguides and resonators with low anomalous dispersion," IEEE Access **9**, 31967–31974 (2021).

44. L. He, Y. Guo, Z. Han, K. Wada, J. Michel, A. M. Agarwal, L. C. Kimerling, G. Li, and L. Zhang, "Broadband athermal waveguides and resonators for datacom and telecom applications," Photonics Res. **6**(11), 987–990 (2018).

45. P. Jean, A. Douaud, T. Thibault, S. LaRochelle, Y. Messaddeq, and W. Shi, "Sulfur-rich chalcogenide claddings for athermal and high-q silicon microring resonators," Opt. Mater. Express **11**(3), 913–925 (2021).

46. C.-L. Wu, Y.-J. Hung, R. Fan, D.-H. Ou, J.-Y. Huang, T.-H. Yen, Y.-J. Chiu, M.-H. Shih, Y.-Y. Lin, A.-K. Chu, and C.-K. Lee, "Tantalum pentoxide (ta2o5) based athermal micro-ring resonator," OSA Continuum **2**(4), 1198–1206 (2019).

47. B. Shen, H. Lin, F. Merget, S. S. Azadeh, C. Li, G.-Q. Lo, K. A. Richardson, J. Hu, and J. Witzens, "Broadband couplers for hybrid silicon-chalcogenide glass photonic integrated circuits," Opt. Express **27**(10), 13781–13792 (2019).

48. B. Morrison, A. Casas-Bedoya, G. Ren, K. Vu, Y. Liu, A. Zarifi, T. G. Nguyen, D.-Y. Choi, D. Marpaung, S. J. Madden, A. Mitchell, and B. J. Eggleton, "Compact brillouin devices through hybrid integration on silicon," Optica **4**(8), 847–854 (2017).

49. K. Vu and S. Madden, "Tellurium dioxide erbium doped planar rib waveguide amplifiers with net gain and 2.8db/cm internal gain," Opt. Express **18**(18), 19192–19200 (2010).